III. RADIO ASTRONOMY*

Academic and Research Staff

Prof. A. H. Barrett
Prof. B. F. Burke
Prof. R. M. Price
Prof. D. H. Staelin
Dr. G. D. Papadopoulos
Dr. J. W. Waters
J. W. Barrett
D. C. Papa

Graduate Students

R. H. Cohen
P. C. Crane
M. S. Ewing
H. F. Hinteregger
P. L. Kebabian
C. A. Knight
K-S. Lam
K-Y. Lo
P. C. Myers
R. K. L. Poon
P. W. Rosenkranz
P. R. Schwartz
J. H. Spencer
A. R. Whitney

A. VERY LONG BASELINE INTERFEROMETRIC STUDY OF THE WATER-VAPOR EMISSION REGIONS IN ORION A

1. Introduction

The H_2O line emission (rest frequency equal to 22235.08 MHz) regions in W49 and Orion A were measured during June 1970, at three radio astronomical receiving stations: the 120 ft antenna of the Haystack Observatory in Tyngsboro, Massachusetts, and the 140 ft and 36 ft antennas of the National Radio Astronomy Observatory at Green Bank, West Virginia, and Kitt Peak, Arizona. The Haystack-Green Bank baseline was 845 km (6.3×10^7 wavelengths), the Green Bank-Kitt Peak baseline was 2940 km (2.2×10^8 wavelengths), and the Haystack-Kitt Peak baseline was 3659 km (2.7×10^8 wavelengths). The maximum fringe spacings for these baselines were 0."0033, 0."00094, and 0."00076.

The portion of the results relating to the angular distribution of radiation in W49 has been reported by Johnston et al.[1] In this report we shall review the results on the structure of Orion A.

2. Experimental Results

The fringe-amplitude spectrum of Orion A, as shown in Fig. III-1 for the Haystack-Green Bank baseline, indicates that there were two prominent features during the June, 1970 observations: one at 3.6 km/s and the other at 9.4 km/s. Although the 9.4 km/s feature appears to be five times stronger than the 3.6 km/s feature, single antenna spectra indicate that the ratio of their amplitudes is approximately 2:1. The difference between the autocorrelation and crosscorrelation spectra results from the position

*This work was supported principally by the National Aeronautics and Space Administration (Grants NGL 22-009-016 and NGR 22-009-421), and the National Science Foundation (Grants GP-20769 and GP-21348); and in part by California Institute of Technology Contract 952568, and the Sloan Fund for Basic Research (M.I.T. Grant 241).

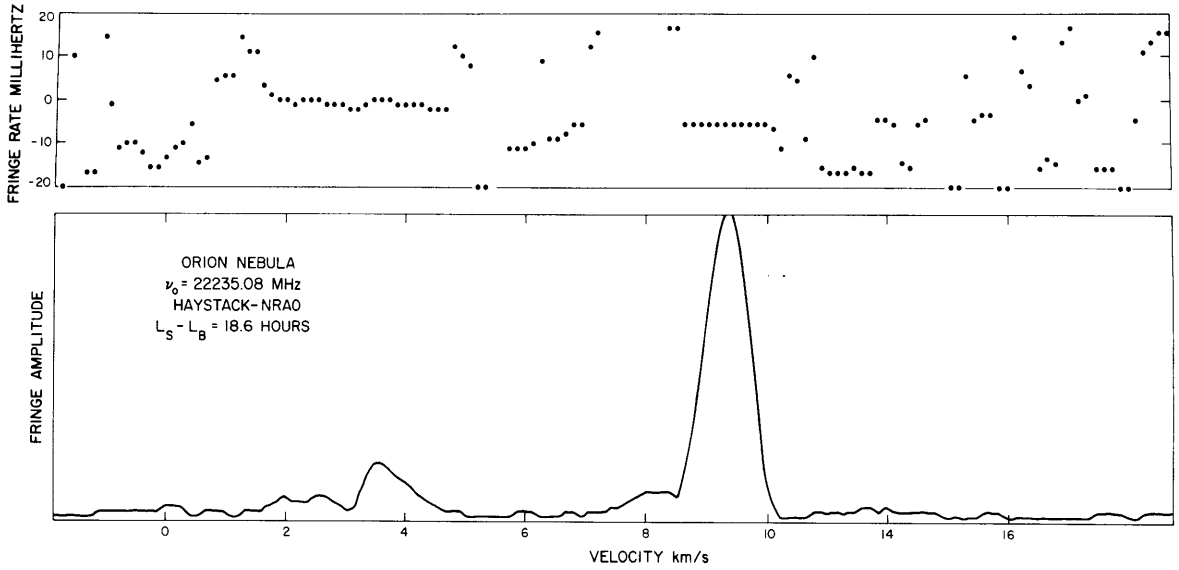

Fig. III-1. Fringe amplitude and relative fringe rate vs velocity for Orion A.

difference between these two features. This position offset translates into a fringe rate offset which must be taken out before the final amplitude spectrum is computed. The data-processing program compensates for the fringe-rate offset of the strongest feature and around it references the offsets of the other features. Therefore the amplitude of a satellite feature with a large relative fringe rate, Δf_R, will be reduced over the integration time of 100 s. By changing the mode of the data-processing operation, we may use the fringe rate of any satellite feature as reference in order to obtain its crosscorrelated peak amplitude.

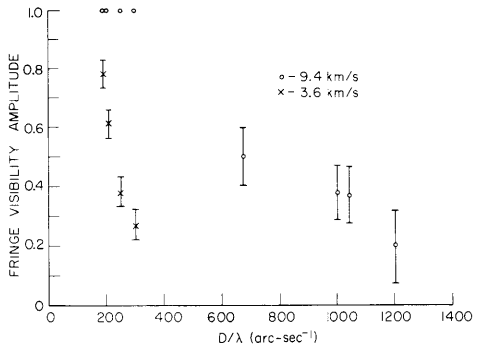

Fig. III-2. Fringe visibility amplitude of the 9.4 km/s and 3.6 km/s features of Orion A.

The crosscorrelated amplitude of the two features discussed above was measured for all three baselines over a period of 3-4 hours. Then the fringe visibility amplitude was calculated from the ratio of the crosscorrelation amplitude to the geometric mean of the

single antenna amplitudes. The results are shown in Fig. III-2. The vertical axis is the fringe-visibility amplitude and the horizontal axis is the projected baseline in number of wavelengths. The 3.6 km/s feature (represented by "x" in the graph) was partially resolved with the Haystack-Green Bank baseline and completely resolved with the two other longer baselines. The 9.4 km/s feature (represented by "o") was unresolved with the Haystack-Green Bank baseline, but it was partially resolved with the others. By assuming a uniform disk model for these features, we find that their sizes are roughly 0.0006 arc-sec for the 9.4 km/s and 0.002 arc-sec for the 3.6 km/s. At 500 parsecs these angular sizes correspond to 0.2 and 0.6 astronomical units, respectively.

The fringe-rate offset, Δf_R, relative to the 9.4 km/s feature is shown in Fig. III-1. The expression for the relative fringe-rate offset is given by

$$\Delta f_R = A[\theta_y \sin \delta_S \sin(L_S - L_B) + \theta_x \cos(L_S - L_B)], \tag{1}$$

where $A = D f_o \Omega \cos \delta_B / c$, with D the baseline length, f_o the sum of the local-oscillator frequencies, c the velocity of light, Ω the rotation of the Earth, δ_B, δ_S, L_B, L_S, the declinations and local hour angles of the baseline and source, respectively, and θ_x and θ_y the relative positions in right ascension and declination, respectively ($\theta_x = \Delta\alpha_S \cos \delta_S$, $\theta_y = \Delta\delta_S$). The constant, A, gives the sensitivity of the fringe rate to position offset and is equal to 20, 72, and 95 mHz per arc-sec for the three baselines. The uncertainty in the fringe-rate measurements because of statistical noise is

$$\sigma_{\Delta f_R} = 4 T_S T_a^{-1} B^{-1/2} \tau^{-3/2} \text{ Hz}, \tag{2}$$

where T_S is the geometric mean of the system temperatures, T_a is the geometric mean of the antenna temperatures, B is the spectral resolution in Hz, and τ is the integration time in seconds. For the 9.4 km/s feature, $T_S/T_a \approx 20$, when it is measured with the Haystack-Green Bank baseline. Then for B = 20 kHz and τ = 100 s we have $\sigma_{\Delta f_R} \approx 0.5$ mHz. The position error is approximately (0.5) (1/20) = 0.025 arc-sec.

Table III-1. Measured fringe rates.

$(L_S - L_B)$ Hours	Δf_R mHz (3.6-9.4 kM/s)
18.6	9.7
19.6	-45.7
21.35	-121.5
21.6	-132.9

The measured relative fringe rates between features 9.4 km/s and 3.6 km/s are listed in Table III-1 with the quantity $(L_s - L_B)$ as parameter. By fitting these measured values of Δf_R to Eq. 1, we obtain the separation between these two features. The results are shown in Fig. III-3 and indicate that the 3.6 km/s feature is 20.3 ± 1.3 arc-sec North and 9.5 ± 0.2 arc-sec West of the 9.4 km/s feature.

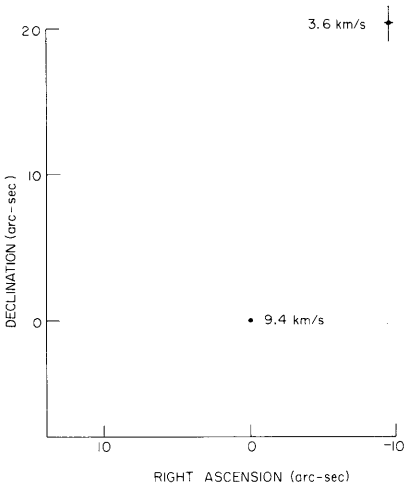

Fig. III-3. Map of H_2O source in Orion (relative to 9.4 km/s feature).

The procedure for calculating the positional offsets and the corresponding errors is presented below.

3. Method for Calculating the Relative Position

The method that we adopted for computing the relative positions was the least-squares fit. We rewrite Eq. 1 in the form

$$y_i = C_{1i}\Delta\alpha + C_{2i}\Delta\delta, \tag{3}$$

where C_{1i} and C_{2i} are the coefficients defined by Eq. 1. This method gives $\Delta\alpha$ and $\Delta\delta$ as follows:

$$\Delta\alpha = \frac{1}{D}\left[\sum_{i=1}^{N} y_i C_{1i} \sum_{i=1}^{N} C_{2i}^2 - \sum_{i=1}^{N} y_i C_{2i} \sum_{i=1}^{N} C_{1i}C_{2i}\right] \tag{4}$$

$$\Delta\delta = \frac{1}{D}\left[\sum_{i=1}^{N} y_i C_{2i} \sum_{i=1}^{N} C_{1i}^2 - \sum_{i=1}^{N} y_i C_{1i} \sum_{i=1}^{N} C_{1i}C_{2i}\right], \tag{5}$$

where N is the number of times that the relative fringe rate was measured, and

$$D = \sum_{i=1}^{N} C_{1i}^2 \sum_{i=1}^{N} C_{2i}^2 - \left(\sum_{i=1}^{N} C_{1i}C_{2i}\right)^2.$$

The variance of $\Delta\alpha$ is given by

$$\sigma^2_{\Delta\alpha} = \langle [\Delta\alpha - \langle \Delta\alpha \rangle]^2 \rangle$$

$$= \langle \Delta^2\alpha \rangle - \langle \Delta\alpha \rangle^2. \tag{6}$$

Let us now call

$$A_{11} = \Sigma\ C_{1i}^2$$

$$A_{22} = \Sigma\ C_{2i}^2$$

$$A_{12} = \Sigma\ C_{1i}C_{2i}. \tag{7}$$

Then $D = A_{11}A_{22} - A_{12}$. The expressions for $\langle \Delta\alpha \rangle$ and $\langle \Delta\alpha^2 \rangle$ are

$$\langle \Delta\alpha \rangle = \frac{1}{D} [A_{22}\ \Sigma\ C_{1i} - A_{12}\ \Sigma\ C_{2i}] \langle y_i \rangle \tag{8}$$

$$\langle \Delta\alpha^2 \rangle = \frac{1}{D^2} \left[A_{22}^2 A_{11} - A_{12}^2 A_{22} + A_{22}^2 \sum_{i \neq j} C_{1i}C_{1j} - 2A_{22}A_{12} \sum_{i \neq j} C_{1i}C_{2j} \right.$$

$$\left. + A_{12}^2 \sum_{i \neq j} C_{2i}C_{2j} \right] \langle y_i^2 \rangle. \tag{9}$$

Since A_{12} is the sum of products of the form $(\sin\phi)(\cos\phi)$, we can assume that $A_{12} \cong 0$. Then the variance, $\sigma^2_{\Delta\alpha}$, becomes

$$\sigma^2_{\Delta\alpha} \cong \frac{1}{A_{22}^2 A_{11}^2} \left[A_{22}^2 A_{11} + A_{22}^2 \sum_{i \neq j} C_{1i}C_{1j} \right] \left[\langle y_i^2 \rangle - \langle y_i \rangle^2 \right]$$

$$\cong \frac{1}{A_{11}^2} \left(\sum_{i,j} C_{1i}C_{1j} \right) \sigma^2, \tag{10}$$

where σ^2 is given by Eq. 1.

Similarly we find the variance of $\Delta\delta$.

$$\sigma^2_{\Delta\delta} \cong \frac{1}{A_{22}^2} \left(\sum_{i,j} C_{2i}C_{2j} \right) \sigma^2. \tag{11}$$

The rms errors in $\Delta\alpha$ and $\Delta\delta$ are found by taking the square root of Eqs. 10 and 11.

G. D. Papadopoulos, B. F. Burke, P. R. Schwartz,
K-Y. Lo, D. C. Papa

[Besides the Research Laboratory of Electronics group other participants in the experiment were K. J. Johnston, S. H. Knowles, and W. T. Sullivan III, of the Naval Research Laboratory, J. M. Moran of the Smithsonian Astrophysical Observatory, C. A. Knight and I. I. Shapiro of the Department of Earth and Planetary Sciences, M.I.T., and W. J. Welch of the University of California, Berkeley.]

References

1. K. J. Johnston, S. H. Knowles, W. T. Sullivan III, B. F. Burke, K-Y. Lo, D. C. Papa, G. D. Papadopoulos, P. R. Schwartz, C. A. Knight, I. I. Shapiro, and W. J. Welch, "An Interferometer Map of the Water-Vapor Sources in W49," Astrophys. J. Letters 166, L21-L26 (1971).

B. RADIO SURVEY OF THE SPIRAL NEBULAE M31 and M33

1. Introduction

Galaxies are composed of stars and gaseous matter. Because the stars once condensed from the interstellar medium, a sound understanding of the gaseous parts of the galaxy is necessary for an understanding of large-scale features. The stars, once condensed, wander uninfluenced by the hydrodynamic forces that act upon the gas. The gas, therefore, more faithfully shows the spiral structure of the galaxy. Unfortunately, it is difficult to study the gross features and distribution of interstellar gas in our own galaxy because of our proximity to the galactic plane. A valuable way of determining the structure of our galaxy is to study other similar galaxies. It is generally felt that two spiral galaxies in the Local Group, the spiral nebula in the constellation Andromeda, M31, and the spiral nebula in Triangulum, M33, are similar to ours in age, size, and structure. For these reasons a program was initiated to study the ionized hydrogen in these two galaxies.

Because the emission from hot ionized gas in the H II regions accounts for only a small fraction of the emission at long wavelengths, observations must be made at short wavelengths to reduce the contribution from nonthermal sources. The emission or absorption of radiation which concerns us occurs at collisions between electrons and ions. An estimate of the expected radiation from an H II region can be made by employing some known properties of H II regions. This estimate will only be valuable for an order-of-magnitude calculation because a nontypical region will cause it to be in error by an order of magnitude. The giant region NGC 604 is one such example. Let us assume an electrostatically neutral region 35 parsecs in diameter heated to a

temperature of 10^4 °K with 10 hydrogen ions per cm^3. From collision theory and Oster[1] we obtain the following expression for the coefficient of absorption. Following Barrett,[2] we find

$$K_\nu = \frac{8N_iN_eZ^2e^6(2\pi)}{3(4\pi\epsilon_o)^3\, cn_i\nu^2(2\pi mkT_e)} \ln\left[\frac{(4\pi\epsilon_o)(2kT_e)^{3/2}}{\gamma^{5/2}\pi m^{1/2}Ze^2\nu}\right].$$

Inserting numerical values in the MKS system of units, we have

$$K_\nu = 9.7 \times 10^{-13} \frac{N_iN_eZ^2}{n_iT_e^{3/2}\nu^2}\left[19.56 + \ln\left(\frac{T_e^{3/2}}{2\pi Z\nu}\right)\right],$$

where

K_ν = absorption coefficient in m^{-1}

N_i = ion number density in m^{-3}

N_e = electron number density

Z = ion atomic number

m = electron mass

c = speed of light

$\gamma = 1.781$

n_i = index of refraction

ν = frequency in hertz

k = Boltzmann's constant

T_e = electron temperature.

The equation above has been derived entirely from classical theories, and this lack of quantum theory limits the expression to electron temperatures below 5.5×10^5 °K. In our case, however, this is of no concern. Using numbers for a receiver wavelength of 7 cm (0.07 m), we find that K_ν is 6.6×10^{-23} m^{-1}. Changing to parsecs, this becomes $\sim 2.1 \times 10^{-7}$ $parsec^{-1}$.

The optical depth is defined by $d\tau = -K_\nu d\ell$. By integration, this becomes $\tau = \int_0^L K_\nu d\ell$. Because this is only an order-of-magnitude estimate, we lose nothing by assuming $\tau = K_\nu L$. For the case that we have assumed, this means τ is 7.2×10^{-5}. The brightness temperature T_b is related to the electron temperature as $T_b = T_e(1-e^{-\tau})$, which for our very small value of τ can be approximated by τT_e. To find the spectral flux density of the radiation at the antenna, we assume that the emitting gas subtends a

solid angle Ω_s. The flux density S_ν is $\int I_\nu \, d\Omega$. For I_ν constant over the solid angle Ω_s, this reduces to $S_\nu = 2kT_b\nu^2\Omega_s/c^2$. For our assumed case of a 35-parsec ionized region in M31, which is at a distance of 650 kparsec, the emission is confined to approximately 120 square seconds of arc. This leads to a typical value of spectral flux density of 3.5×10^{-3} flux units. A flux unit is 10^{-26} W/m^2/Hz. The interferometer at the National Radio Astronomy Observatory can reach noise levels lower than this in two days of observing. A region smaller or hotter than the one represented here would be detected with ease. Large sources are resolved and therefore are hard to recognize in a noisy or crowded field. This might mean that a program using this instrument would be limited to observing bright knots in H II regions of these galaxies.

The dual-frequency interferometer at the National Radio Astronomy Observatory is used in its dual-frequency mode and observations are made at both 2695 MHz (11.1 cm) and 8085 MHz (3.7 cm) in order to obtain a spectral index for any observed source. Because only two of the planned observing periods have been conducted thus far, very preliminary results are presented in this report. The results so far have been encouraging. Further observations are scheduled in October, and are in the planning stage for later times.

2. Observations

In March 1971, eleven fields in M31 and M33, plus two comparison areas of sky chosen at random were observed. The telescopes were spaced to provide baselines of 0.9, 1.8, and 2.7 km which correspond to spacings up to 24,300 λ at 11.1 cm and 73,000 λ at 3.7 cm. These baselines produce interferometer fringe spacings of 8.″2 and 2.″7, respectively. In May 1971, three new fields were examined while six of the old ones were omitted, at least temporarily. The purpose of these two sessions was to observe as many interesting fields in the two galaxies as possible, while also spending enough integration time on a few selected fields to reach low noise levels quickly. The areas of coverage were selected after examining the red plates of the Palomar Sky Survey. A photograph of M31 taken in Hα light by Arp[3] was used to help select emission regions in M31. Detected radio sources are compared with the 5C3 catalog of M31 by Pooley,[4] or with the regions of classical H II appearance found in M33 by Carranza et al.[5]

3. Data Reduction

Thus far all data from the interferometer have been reduced and examined. Standard computer programs from the NRAO computer facility in Charlottesville, Virginia, are being used. Since July 1971 copies of these programs brought to M.I.T. have been working, which will result in convenience in operation as well as lower travel costs. Specialized computer programs written specifically for this observing program can be

included easily in the program library because they are operated on the same computer and are completely compatible.

The data processing at the present time comprises several programs which may be run sequentially to read the interferometer tape, delete bad data, correct the baselines, calibrate the amplitude and phase, and finally perform a Fourier transform on the data to produce a map of a region of sky. Additionally there are several utility programs which may be used at any stage of processing to display the data in several formats.

4. Results

Much time has been spent converting the interferometer program library from the NRAO computer system to the IBM 360/65 operating on release 20.0 which is in present use at the Information Processing Center of M.I.T. The primary effort has been in writing and modifying programs, but preliminary maps of all fields at both wavelengths have been made. The maps are normalized to the amplitude of the strongest source if it is not resolved. A resolved source requires care to "integrate the pieces" to obtain the total amplitude, and this has been done for only one map. This means that while we do have coverage of the nuclear regions of M31 and M33 and the rich southern spiral arm of M33 mentioned by Carranza et al., these regions are so large and full of weak radio sources that the small amount of data collected on the three baselines cannot produce a good map. Since we had expected this difficulty, we planned observations to produce a full aperture synthesis using many baseline configurations. With only the three baselines and, in some cases, incomplete hour-angle coverage, there are, at present, only pieces of three ellipses of U-V plane space covered that can be used to perform Fourier transforms. While this is enough coverage to make estimates of point sources, nothing can be said yet about the complex fields. Furthermore, a highly resolved source appears very similar to Lorentz noise.

At present, the positions of the indicated point sources are being compared with the positions of the radio sources in the 5C3 catalog, the emission regions of Carranza et al., or the HII regions of M31 listed by Baade and Arp.[6] Because all three of the source lists have positions listed in different coordinates, this comparison is a slow process and the danger of making an error is great. Thus far we have found a correspondence between one source and 5C3.141a. The spectral index we obtained and the one calculated from the cataloged data are -0.67 and -0.72, respectively. At 11.1 cm the position is unresolved, but with the additional resolution at 3.7 cm, the source is partially resolved and suggests a size of 13.5 parsecs using the distance of M31 as 650 parsecs. The other detected sources have not yet been related to cataloged positions. More data covering the complex fields will lead to more detected sources.

J. H. Spencer

References

1. L. Oster, Rev. Mod. Phys. 33, 525 (1961).
2. A. H. Barrett, Department of Physics, M.I.T., unpublished class notes, 1970.
3. H. C. Arp, Astrophys. J. 139, 1045 (1964).
4. G. G. Pooley, M. N. Roy. Astron. Soc. 144, 101 (1969).
5. G. Carranza, G. Courtès, Y. Georgelin, G. Monnet, and A. Pourcelot, Ann. Astrophys. 31, 63 (1968).
6. W. Baade and H. C. Arp, Astrophys. J. 139, 1027 (1964).

C. STELLAR INTERFEROMETER

During this quarter we have been working on the construction of the signal processor and it is now nearing completion. As previously reported,[1] the MOS shift registers in the signal processor can be used with the substrate at +3.6 V by translating the output voltages of the RTL gates from +2.6 and +.4 to +1.4 and −0.8. Since the input of the shift registers is capacitive, nominally 4 pF, this can be done by the resistive voltage divider shown in Fig. III-4a. When time delays are critical, the 9.1 kΩ resistor can be replaced by two forward-biased diodes. Several circuits have been built using the shift registers with +3.6 V on the substrate, and all work correctly.

When the clock voltages for 10 or more shift registers are supplied from a single clock buffer, the inductance of ordinary wiring and the ~500 pF capacitance of the shift registers can cause ringing. To eliminate this, the clock signals are distributed by a parallel-plate transmission line. A convenient way of making such a transmission line is to cut a strip of the required length from two-sided, 1/16 in. thick, G-10 etched board 1/4 in. wide. The strip fits exactly between the contacts of printed circuit sockets with the widely used 0.156 in. contact spacing. Since the displacement current through the clock capacitance flows, for the most part, to the substrate, we wire the transmission lines as shown in Fig. III-4b. This isolates the current in the clock lines from the rest of the circuits in the processor, and minimizes a potentially troublesome source of noise.

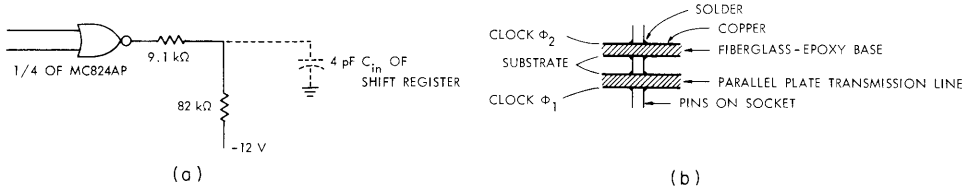

Fig. III-4. (a) Level translator.
(b) Clock distribution wiring.

In building and testing the signal processor, a convenient, low-level light source has often been required as a test signal for the phototubes. Light-emitting diodes, which are now available at low cost, work particularly well. They can be made from GaAs, with light output at 9000 Å in the infrared, from $GaAs_xP_{1-x}$, with light output around 6700 Å, and from GaP. The GaP diode used in these experiments radiates in two bands, one at 5600 Å, which contains most of the power, and one at ~6700 Å. The specified junction capacitance is typically 200 pF, and the rise time of the light output < 10 ns.

The light-emission process in these diodes is quite complex, and in order to use them for the present purpose, we need a simplified model of their behavior. Manufacturers normally specify the light output as a function of current, but these current and light levels are far larger than required in a low-level light source for testing photomultiplier tubes. Also, the light output is really only a function of one component of the current, the current arising from carriers that recombine and radiate light in the process.

Because of the many recombination processes (cf. reference 2), diodes are characterized by the V-I relation $I = I_s \exp[(qV/nkT)-1] \approx I_s \exp(qV/nkT)$ where, for an ideal diode n = 1 and for real diodes, n is typically between 1 and 2. Among the light-emitting diodes used for these experiments, typical values are n = 2 and $I_s = 2 \times 10^{-18}$ a. At high currents observations will depart from this relation because of series resistance in the bulk material of the diode, and heating of the junction.

We measured the light output vs voltage characteristic of the light-emitting diodes listed below. The Motorola diode was measured with a reverse-biased silicon photodiode.

Motorola	MLED-900	GaAs	9000 Å
Monsanto	MV-1	$GaAs_xP_{1-x}$	6100 Å
Monsanto	MV-2	GaP	5600 Å 6700 Å
Monsanto	MV-10B	$GaAs_xP_{1-x}$	6700 Å
Hewlett-Packard	H-P 5082-4400	$GaAs_xP_{1-x}$	6600 Å

The Monsanto and Hewlett-Packard diodes were measured with a photomultiplier tube.

In all cases, the light output obeyed the characteristic $L = L_o e^{V/V_o}$, and $V_o = 25 \pm 1$ mV except for the IR emitter, where $V_o = 25 \pm 3$ mV because of less accurate voltage measurements in that experiment. It appears that the component of current causing the light output varies as $e^{qV/kT}$, even though the total current varies as $e^{qV/nkT}$, $n \approx 2$. A typical value of L_o corresponds to 1.5×10^{-12} photons detected per year.

We have not yet measured the temperature dependence of L_o. The manufacturer's data sheet specifies light output vs temperature at constant current, and a -2 mV/°C temperature coefficient of forward voltage. If we use these values and the measured $e^{V/25\,mV}$ characteristic, it appears that L_o will increase ~7%/°C.

If the diode is to be used conveniently as a calibrated light source, one important parameter to determine is the highest voltage that can be applied before a correction for series resistance is required. We measured this with a filter over the diode to reduce the counting rate of the photomultiplier, and with a low-duty ratio to prevent excessive heating of the junction. We also need to know the lowest useful voltage. Arbitrarily taking that level to be 1 photon detected per second, we get an operating range in which the diode may be used as a voltage-controlled light source. For the H-P diode and the MV-10B diode, this range is 7.5 decades of light output. If a phototube with better red sensitivity were used, it would be at least 8.5 decades (the photomultiplier had a bi-alkalai cathode). For the MV-2 diode, the range is only ~5 decades, because of the much higher series resistance.

We conclude that light-emitting diodes are a convenient voltage-controlled light source. By varying the applied voltage, the light output can be changed exponentially over many decades without the great inconvenience of a calibrated set of dense filters. For high-precision measurements, the temperature must be kept constant, but the temperature dependence is not so great that this is a major obstacle. Unlike tungsten lamps, light-emitting diodes exhibit negligible aging; changes occur only on a time scale of 10^5 h, even at the typical current levels for such uses as pilot lights. Also unlike that of tungsten lamps, the spectrum of light from the diode does not change significantly when the level is changed. All of these properties make light-emitting diodes excellent transfer standards for precision radiometry at low light levels. In fact, they might even be used as a primary standard; one could intercompare the light outputs of a set of diodes, as is done with the voltages of standard cells.

1. Duplicating Filters

In a previous report[3] we described a family of digital filters that used decimation of sampling rate, with the invariance property that when a given reduction in sampling rate was directly realized, the transfer function was identical to that of a cascade of filters of the same structure. In these filters the product of the sampling rate reductions was equal to the directly realized reduction. In order to understand the operation of these filters, and of the filters in a new family that we shall describe, three central ideas must be kept in mind.

1. When dealing with filters that reduce the sampling rate, the impulse response, ${}_rh_n$, represents the response at sample 0 of the output to an input of 1 at sample -n of the input. Sample 0 of the input is simultaneous with sample 0 of the output, and r is

the factor by which the sampling rate is reduced.

2. When two filters that reduce the sampling rate are cascaded, as shown in Fig. III-5a, the resulting impulse response is given by

$$ {}_{r_1 r_2}h_b = \sum_{j=0}^{[b/r_1]} {}_{r_2}h_j \cdot {}_{r_1}h_{b-r_1 j} = {}_{r_1}h_b[*]\,{}_{r_2}h_b, \qquad (1) $$

where $[b/r_1]$ means the largest integer in b/r_1, and is used because the filters are causal, and thus ${}_{r}h_{b<0} = 0$. This operation, denoted $[*]$, is the analog of convolution for filters with decimation of sampling rate. Note that, since the two filters operate at different sampling rates, there is a definite order associated with Eq. 1; unlike the case of discrete convolution to which this reduces when $r_1 = 1$, it is not possible to change variables so as to interchange the roles of the two filters in the summation.

In general, the operation $[*]$ is not commutative. As an example, let ${}_{r_1}h_b = 1, 2, 3$, ${}_{r_2}h_b = 3, 2, 1$, and $r_1 = 2 = r_2$. Then

$$ \begin{array}{rl} {}_{r_1}h_b[*]\,{}_{r_2}h_b & = 3 \cdot (1,\ 2,\ 3\qquad\quad\ ) \\ & + 2 \cdot (\quad\ 1,\ 2,\ 3\quad\ ) \\ & + 1 \cdot (\qquad\quad 1,\ 2,\ 3\ ) \\ \hline & = \quad 3,\ 6,\ 11,\ 4,\ 7,\ 2,\ 3 \end{array} $$

$$ \begin{array}{rl} {}_{r_2}h_b[*]\,{}_{r_1}h_b & = 1 \cdot (3,\ 2,\ 1\qquad\quad\ ) \\ & + 2 \cdot (\quad\ 3,\ 2,\ 1\quad\ ) \\ & + 3 \cdot (\qquad\quad 3,\ 2,\ 1\ ) \\ \hline & = \quad 3,\ 2,\ 7,\ 4,\ 11,\ 6,\ 3 \end{array} \qquad \neq {}_{r_1}h_b[*]\,{}_{r_2}h_b. $$

3. The duplicating property does not pertain to any particular impulse response, but rather to the structure, that is, the circuit or other algorithm by which a family of impulse responses is generated. Let the algorithm A, for every integer $r \geq 2$, generate the impulse response ${}_{r}h_b$. A is said to have the duplicating property iff, for all $r_1, r_2 \geq 2$, ${}_{r_1 r_2}h_b = {}_{r_1}h_b[*]\,{}_{r_2}h_b$. Note that in Eq. 1, two of the three filters were arbitrary, but for A to have the duplicating property, all three must be generated by the algorithm A.

Two immediate consequences of this definition are that if two filters are generated by an algorithm with the duplicating property, they commute when they are cascaded; and when duplicating filters are used to reduce the sampling rate, all possible cascade realizations of a given total rate reduction have the same impulse response.

We have previously[3] derived a duplicating filter (reprinted in this report as Fig. III-5b). In order to determine whether the duplicating property was unique to the filters

derived previously, we decided to look for other algorithms which have the duplicating property.

Our interest in this problem arises because we are not studying any particular impulse response, $_{r}h_{b}$, but the algorithm generating $_{r}h_{b}$ for all $r \geq 2$. Hence there

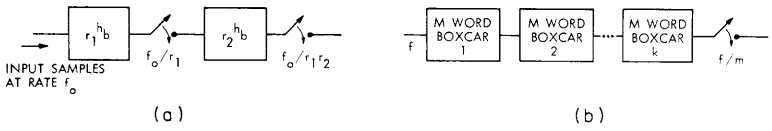

Fig. III-5. (a) Cascade of two filters with decimation of sampling rate.
(b) Unit cell of duplicating filter previously derived.[3]

seems to be no way to solve Eq. 1 directly to get all, or in fact any, of the required algorithms, or to show that there are no others. The method of solution has been to study the properties of the family of duplicating filters of Fig. III-5b and by analogy decide on a plausible algorithm, but one with almost no restrictions on its properties except causality. Next, by considering specific cases out of the infinite number of equations constituting Eq. 1, the algorithm is made more specific, until only a single free parameter remains, which is the analog of k in Fig. III-5b. The next step would ordinarily be to prove or disprove that the algorithm has the duplicating property, but this has not yet been done. As an alternative, the properties of the algorithm have been studied numerically.

In this case, the numbers involved are, in general, irrational, and so the results of a numerical investigation of this kind are in no sense rigorous. Nevertheless, in this kind of problem, a numerical answer is likely to be either exactly right, except for the limited number of digits in the calculation, or entirely wrong, with an error comparable to the function that is being studied. Thus the numerical calculation will either provide a counterexample, or reveal an error so small that the relation that is being tested may be assumed to be true.

In the present problem, duplicating filters have been numerically generated and tested in Eq. 1 to see if, when $_{r_1}h_b$ and $_{r_2}h_b$ are generated by the algorithm that is under study, $_{r_1r_2}h_b$ is also generated by that algorithm. The discrepancy between the two sides of Eq. 1 has been found to be $< 10^{-6}$ of the value of the function. This must be expected from the double-precision arithmetic of the computer that we used, and the way in which the function was calculated; our calculations required repeated use of the small difference between two large numbers.

From this result we see that, at least as a working hypothesis, the algorithm may

be considered to have the duplicating property, and the hypothesis merits further investigation, whereas time spent trying to prove that it does not have the duplicating property would probably be wasted. The availability of large digital computers has greatly increased both the potentialities and the facility of this technique. Correspondingly greater caution is required in dealing with the results obtained. With this caveat, let us proceed to a new family of duplicating filters.

Consider one of the filters in the family defined by Fig. III-5b. Let the rate reduction, m, become very large, and the actual time between input samples, τ, become very small, so that $m\tau$, the time between output samples, T, stays constant. Let the value of each point in the impulse response be multiplied by 1/m; this does not change the duplicating property, and the result is that, for very large m, the response approaches that of a filter formed from continuous-time boxcar integrators, the output being sampled at intervals of T, the length of one of the boxcar integrators.

Note that for any algorithm with the duplicating property the resulting filters ${}_rh_b$ may be multiplied by a normalizing constant, r^q, without changing the duplicating property; q may be any finite number, and hereafter will be 0.

Although there is no obvious reason why all duplicating filters must approach a physically reasonable limit when the rate reduction and input rate are changed in this way, a logical place to look for other algorithms with the duplicating property is among those which approach a reasonable limit. The algorithm should in some way be defined by the limiting continuous function, since this will permit us to use Eq. 1 to solve for the properties (thus far unspecified) of that function. An obvious way to do this is to let

$$ {}_rh_b = h\left(\frac{1+b}{r}\right), \tag{2}$$

where h(x) is the limiting continuous function. Note that, in general, the duplicating filters of Fig. III-5b are not obtained in this way, but the case k = 2, as well as the case k = 1, does correspond to this kind of sampling provided that the corresponding continuous-time boxcar integrator is defined as 1 at the end point x = 1.

By letting r_1 and b approach ∞ so that $(1+b)/r_1 \to x > 1$, Eq. 1 reduced to

$$h(x/r_2) = h(1/r_2)\, h(x) \qquad \text{for all } r_2 \geq 2. \tag{3}$$

If we neglect the physically unreasonable case $h(1/r_2) = 0$ and nonzero at other values of x, this means that $h(x) = x^{\alpha}$, $0 < x < 1$. Also, $h(x<0) = 0$ because the filter must be causal, and $\alpha > 0$ because $\alpha < 0$ corresponds to a physically unreasonable h(x), and $\alpha = 0$ corresponds to the special case of a single boxcar integrator. Since h(x) must be continuous, h(1) = 1.

Next, let $r_2 = 2$, r_1 and b approach ∞ so that $(1+b)/r_1 \to x$, $1 < x < 2$. Now

$$h(x/2) = h(1/2)\, h(x) + h(1)\, h(x-1)$$

$$h(x) = (h(x/2) - h(1)h(x-1))/h(1/2) = 2^{a}((x/2)^{a} - 1 \cdot h(x-1)$$

$$h(x) = x^{a} - 2^{a} h(x-1). \tag{4}$$

Continuing in the same way for all other values of r_2, we find

$$\ell - 1 < x < \ell, \qquad h_{a}(x) = x^{a} - \sum_{j=1}^{\ell-1} (j+1)^{a}\, h_{a}(x-j), \tag{5}$$

where the notation has been changed slightly, so that the designation of the function includes the free parameter a.

It may readily be verified that $h_{a}(x = 2, 3, 4, \ldots) = 0$, $h_1(x)$ is the triangle function corresponding to k = 2 of the duplicating filters of Fig. III-5b, and $h_o(x)$ is a single box-car, corresponding to k = 1.

For some purposes it is convenient to make the following changes of variables in (5): $k = \ell - 1$, $y = x - k$. Now

$$k = 0 \qquad h_{a}(k, y) = y^{a}$$

$$k = 1 \qquad h_{a}(k, y) = (y+1)^{a} - 2^{a} y^{a}$$

$$k = 2 \qquad h_{a}(k, y) = (y+2)^{a} - 2^{a}(y+1)^{a} + (4^{a} - 3^{a}) y^{a}$$

and, in general,

$$h_{a}(k, y) = \sum_{m=0}^{k} (y+k-m)^{a}\, C_{m},$$

where

$$C_{o} = 1 \quad \text{and} \quad C_{m} = \sum_{i=1}^{m} -(i+1)^{a}\, C_{m-i}$$

It is now easy to verify that for $a = 2$ the function oscillates, $h_2(k, y) = \pm 4y(y-1)$, +for odd k, -for even k, $k \geq 2$. Also, $C_o = 1$, $C_1 = -4$, $C_2 = +7$, $C_3 = C_5 = C_{odd} = -8$, $C_4 = C_6 = C_{even} = +8$.

To study numerically the properties of $h_{a}(x)$, typical values were computed using

Eq. 5. The values of a were 0.25, 0.50, 0.75, 1.25, 1.50, and 1.75. The step size in x was 1/16, and the range in x was from 0 to 64. Next, the duplicating property was tested by sampling $h_a(x)$ as specified in Eq. 2, for various values of r_1 and r_2, and these samples were used in Eq. 1 to find ${}_{r_1 r_2}h_b$, which was then compared with ${}_{r_1 r_2}h_b$, as found by directly sampling $h_a(x)$. The values of r_1 and r_2 were, respectively, 2, 4, 8, 4 and 2, 2, 2, 4. The largest discrepancy was $< 10^{-6}$ of the value of the function. The case of $a = 2.5$ was also investigated in this way, and again the discrepancy was negligible compared with the function. This result is of particular interest because $h_{2.5}(x)$ grows exponentially, hence the duplicating property seems to be independent of whether the resulting filters are stable.

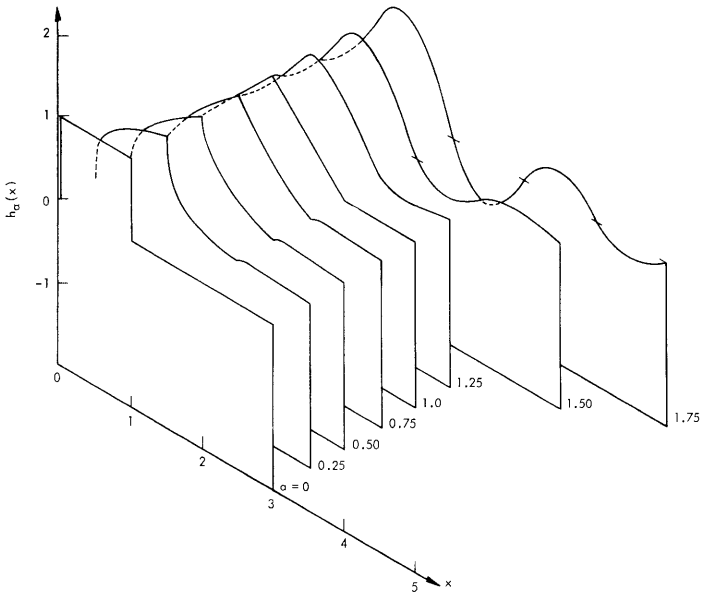

Fig. III-6. Isometric representation of $h_a(x)$.

The general appearance of the functions $h_a(x)$ is shown in Fig. III-6, for small values of x. Figures III-7 through III-10 are semi-log graphs of some of these functions. Note especially the zero in $h_{1.25}(x)$ between x = 5 and x = 6. This is definitely not a computational artifact, since the maximum discrepancy between the duplicate filter and the original is $< 5 \times 10^{-15}$ in this range.

Figure III-11 shows the maxima of $|h_a(x)|$ for moderate values of x. Note that the behavior is approximately exponential, the exponent varying roughly as $(a-2)$. The case $a = 2$ is not drawn, but its behavior (oscillating with no growth or decay) corresponds to an exponent of 0 at $(a-2) = 0$. The exponential decay of these functions does not

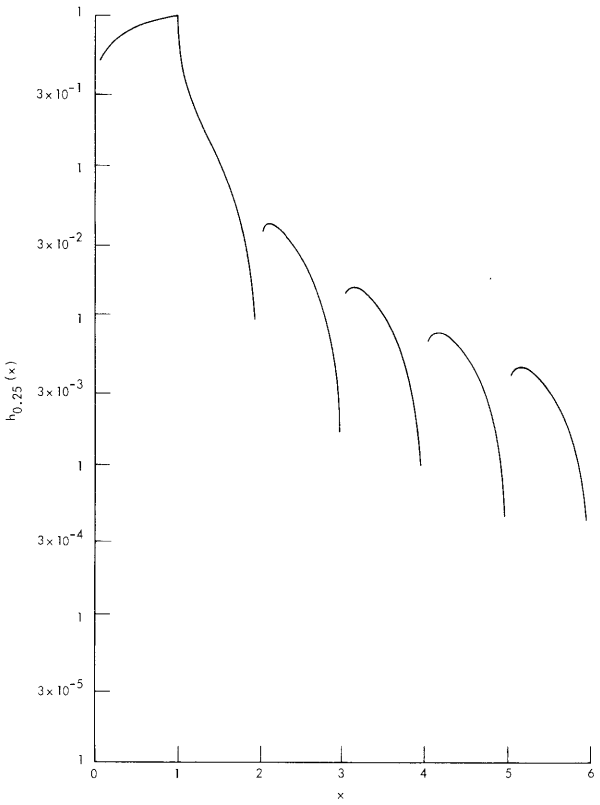

Fig. III-7. The function $h_{.25}(x)$.

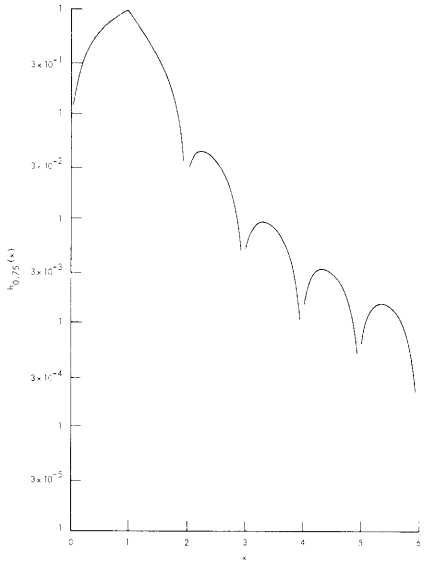

Fig. III-8. The function $h_{.75}(x)$.

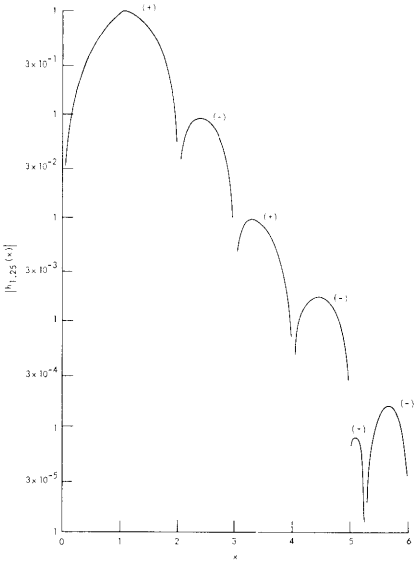

Fig. III-9. The function $h_{1.25}(x)$.

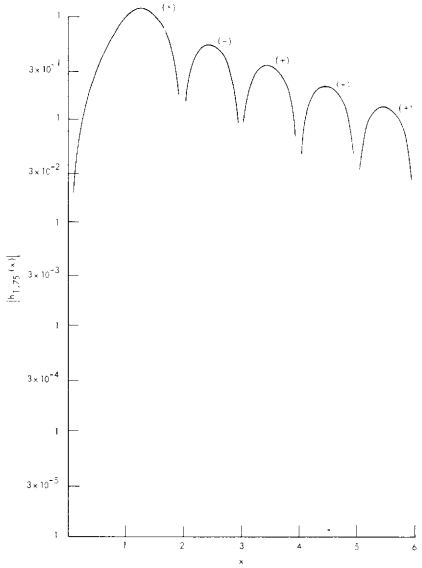

Fig. III-10. The function $h_{1.75}(x)$.

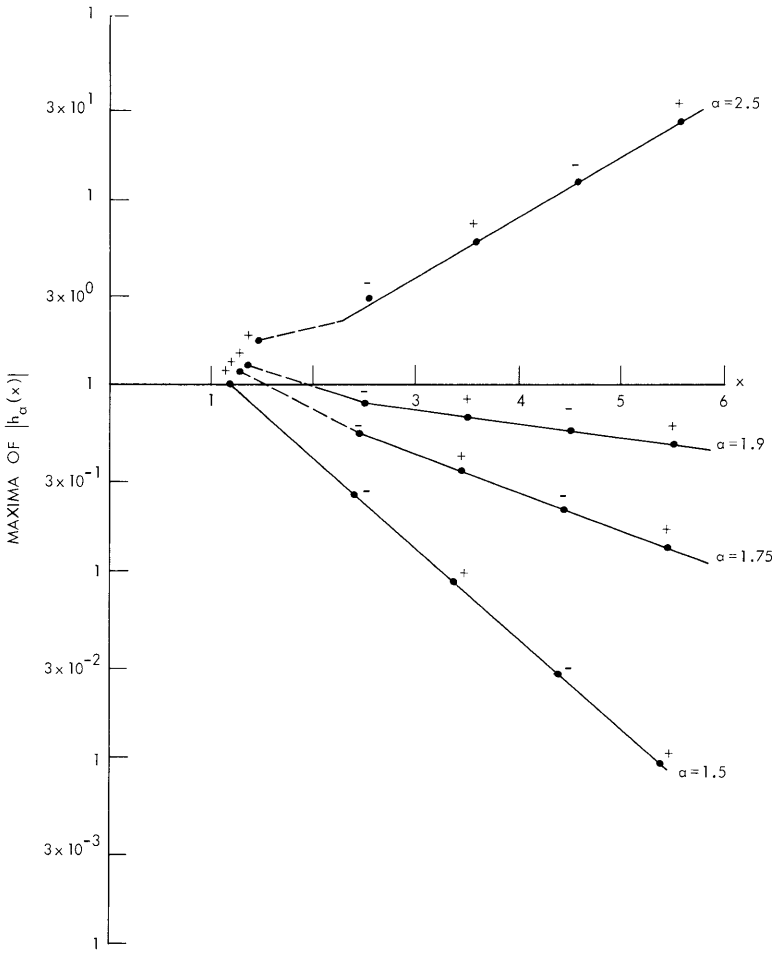

Fig. III-11. Maxima of $|h_\alpha(x)|$ for moderate values of x.

continue indefinitely, however. At some point the $e^{-\beta x}$ decay changes to $x^{-\gamma}$ decay, and instead of a single loop in each unit interval, there are two. For $\alpha \leq 1.25$ we presume that the exponential decay is too rapid for this transition to be evident. The $x^{-\gamma}$ behavior of $h_\alpha(x)$, is shown in Fig. III-12. Figure III-13 shows β and γ vs α. For $\alpha = 1.5$ and 1.75, both the positive and negative extrema are graphed, but for $\alpha = 1.25$, only the minima are shown because the maxima and zeros occur between 0 and 1/16, the size of the computation, except for x between 5 and 6.

For $\alpha < 1$, there is no region where exponential decay is observed, and, unlike the cases with $\alpha > 1$, the loops of the function do not have alternating signs but are always positive. (See Figs. III-14 and III-15.)

To study the transition from exponential to power-law decay, the values of $h_\alpha(x)$ in the vicinity of extrema and zeros, as found with steps of 1/16 in x, were recalculated with smaller steps. Figure III-16 shows the locations of these roots as a function of [x], for different values of α.

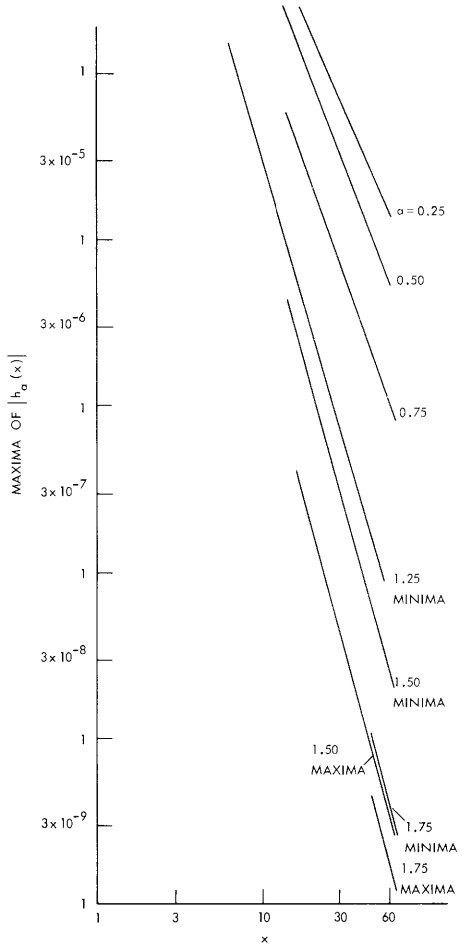

Fig. III-12. Extrema of $h_\alpha(x)$ for large values of x.

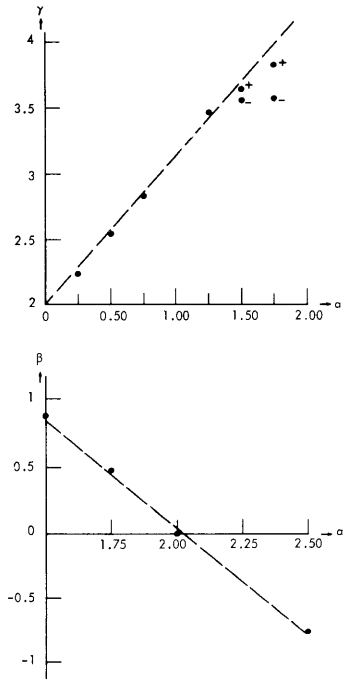

Fig. III-13. β and γ as functions of α.

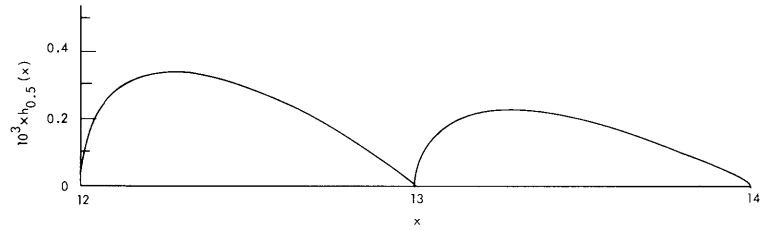

Fig. III-14. The function $h_{.5}(x)$ between x = 12 and x = 14, linear scale.

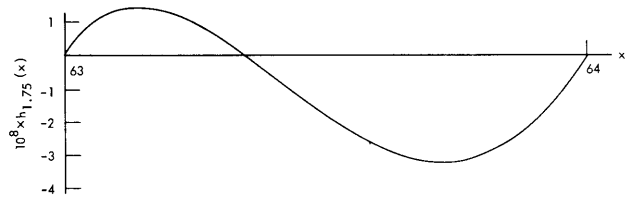

Fig. III-15. The function $h_{1.75}(x)$ between x = 63 and x = 64, linear scale.

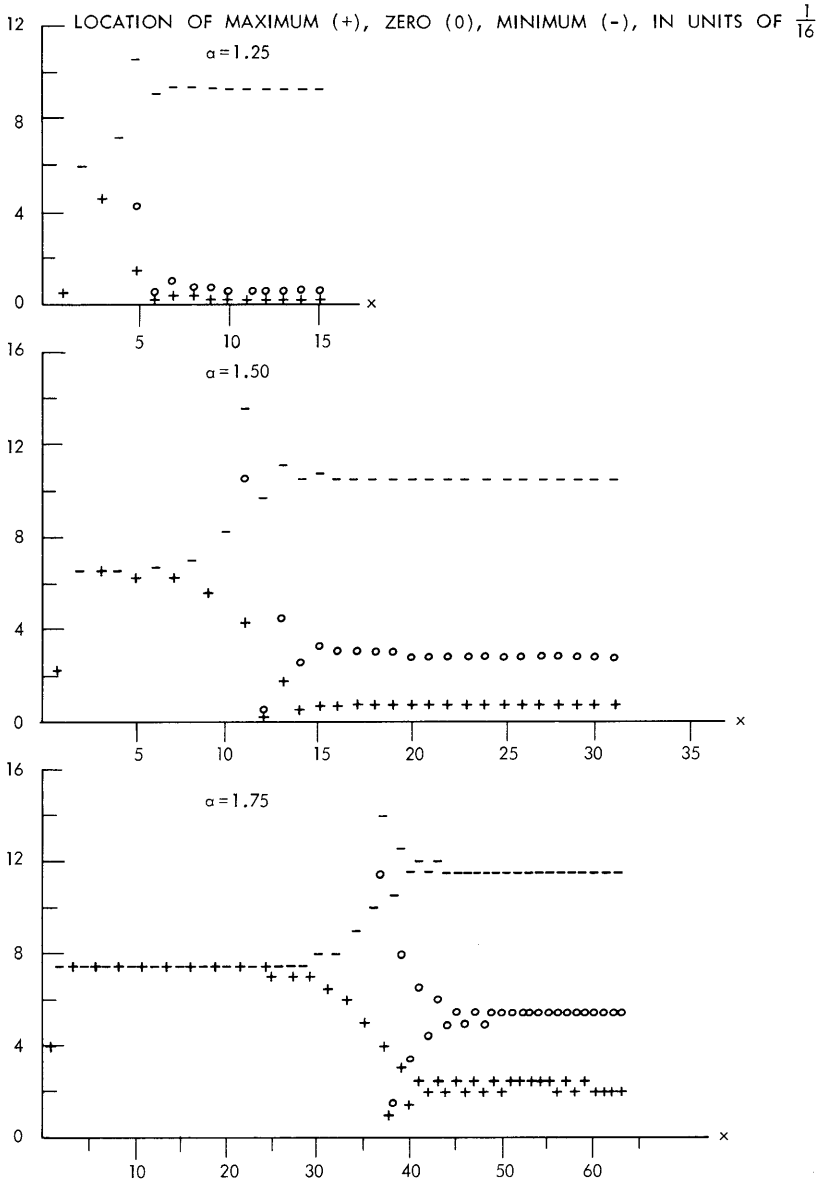

Fig. III-16. Maxima, zeros, and minima of $h_\alpha(x)$.

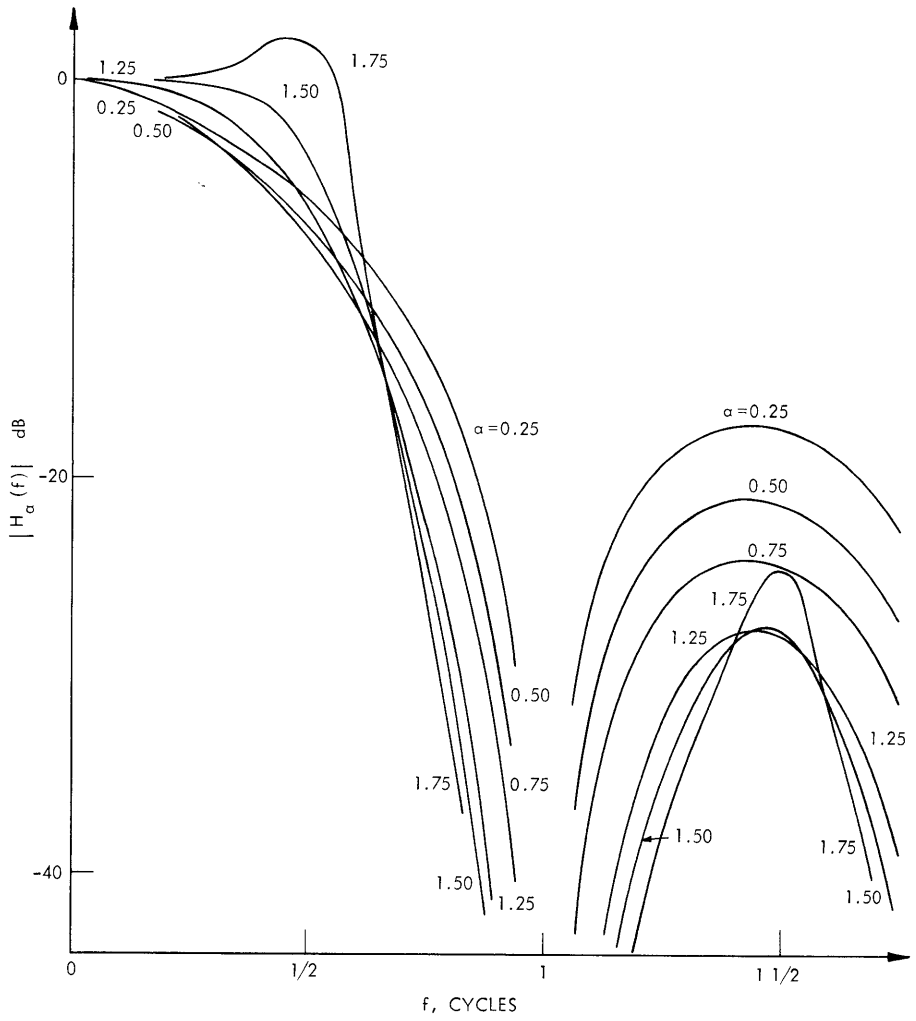

Fig. III-17. $|H_\alpha(f)|$, the Fourier transform of $h_\alpha(x)$.

Figure III-17 shows the Fourier transform, $H_\alpha(f)$, of $h_\alpha(x)$, and Fig. III-18 shows the sidelobe amplitudes. Note that, although H(f) must vary smoothly from $(\sin \pi f)/\pi f$ for $\alpha = 0$ to $\left(\frac{\sin \pi f}{\pi f}\right)^2$ for $\alpha = 1$, it does not vary uniformly, that is, the curves cross each other. The $H_\alpha(f)$ filters are not especially good filters. This is not surprising, and indeed the first family of duplicating filters were also poor filters by the usual criteria of fast rolloff or low sidelobes, and their practical importance is a factor of the very simple and economical way in which they can be realized. The filters $h_\alpha(x)$, on the other hand, can only be realized by direct convolution with a table of stored values or in some equivalent way, and since the duration of $h_\alpha(x)$ is infinite and the coefficients are irrational, the result would only be an approximation of a duplicating filter. Unlike the first family of duplicating filters, the $h_\alpha(x)$ filters do not have a center of symmetry, and hence the phase response is not linear.

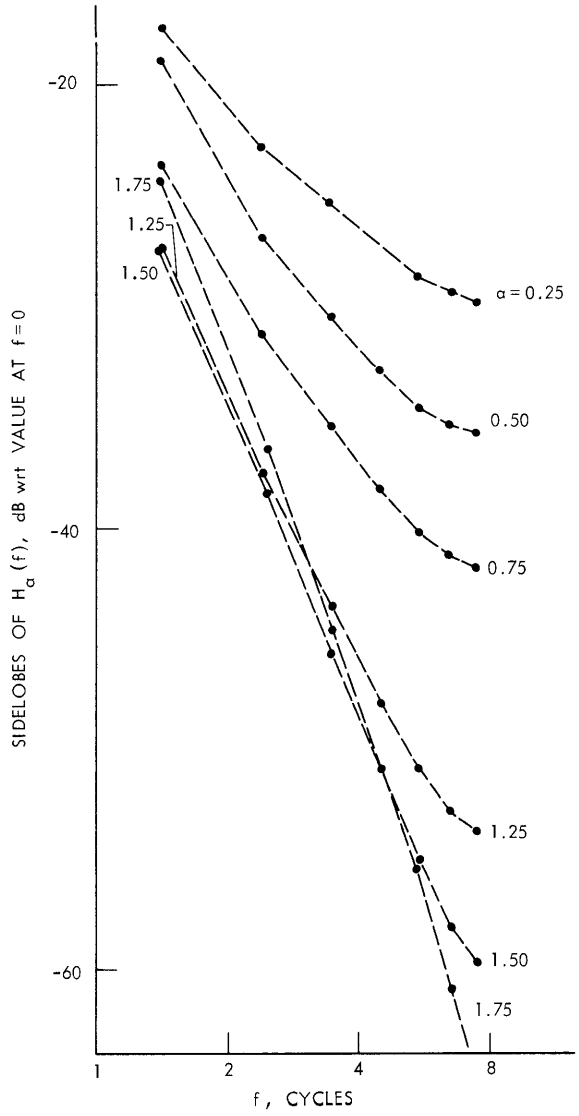

Fig. III-18. Sidelobes of $H_\alpha(f)$.

For these reasons, $h_\alpha(x)$ does not generate a practical filter. The sequence of functions $h_\alpha(x)$ provides a reasonable way of going from a single boxcar integrator to a cascade of two, and thus $h_{.5}(x)$ is in a sense the impulse response of one-and-a-half boxcar integrators, a result comparable to the sound of one hand clapping. Its importance is in demonstrating that the previously found family is not unique. In this connection, note that all of the derivations in our previous report[3] continue to apply when S_m, S_ℓ, and $S_{m\ell}$ of Fig. I-5 in that report are duplicating filters obtained by sampling $h_\alpha(x)$. Note also that there are two distinct ways for the resulting filter to have a limiting impulse response (as the sampling rate and rate reduction are increased)

varying initially as x^p, $p > 1$, by using $0 < \alpha < 1$ and $[p]$ boxcars, or by using $1 < \alpha < 2$ and $[p]-1$ boxcars. Hence, if filters within a family are arranged according to p, there are four distinct, though closely related, families of duplicating filters.

It should now be clear that duplicating is essentially a time-domain property: it persists for $\alpha > 2$, in which case $h_\alpha(x)$ does not have a Fourier transform. Also, while it is quite simple to derive $h_\alpha(x)$, it is difficult to imagine deriving $H_\alpha(f)$ from any sort of frequency-domain arguments. Finally, the interesting time-domain properties such as the change from exponential decay with frequency 0.5 to power-law decay with frequency 1 are quite invisible in the frequency domain, where the only effect is a very slight shift in the positions of the zeros.

For further investigation, there remains the proof that the new family of filters in fact duplicates, and beyond that there is the study of the other properties of $h_\alpha(x)$. Whether these matters are worth studying will depend on the answer to a more important question. Are there algorithms with the duplicating property which are not, like the four present ones, closely related to boxcar integrators? If so, then it will be clear that duplicating is a relatively common property of filters using decimation of sampling rate, but if not, then the study of the properties of $h_\alpha(x)$ may help to clarify just how widespread the duplicating property is. Another problem is whether duplicating filters are the only filters with decimation of sampling rate which are commutative when they are cascaded.

The author wishes to thank R. K. L. Poon for helping with the programming.

P. L. Kebabian

References

1. P. L. Kebabian, Quarterly Progress Report No. 102, Research Laboratory of Electronics, M.I.T., July 15, 1971, pp. 25-27.
2. Hewlett-Packard Technical Staff, Electronics, Vol. 41, No. 18, pp. 76-77, 1968.
3. P. L. Kebabian, Quarterly Progress Report No. 101, Research Laboratory of Electronics, M.I.T., April 15, 1971, pp. 1-11.

D. INFRARED AND MICROWAVE TRANSMISSION IN THE ATMOSPHERE OF VENUS

1. Introduction

The study of radiative transfer in the atmosphere of Venus is more meaningful now that in situ measurements by USSR spacecrafts have provided more knowledge of physical conditions on the planet. This knowledge, combined with recent terrestrial laboratory experiments performed under similar conditions, enables estimation of brightness temperature and weighting functions in both infrared and microwave regions. There are

still areas of uncertainty, particularly concerning the dense cloud layer that completely covers Venus. We therefore present different sets of results for various cloud parameters that seem reasonable. For simplicity, we assume that cloud drops are sufficiently smaller than the observation wavelength so that scattering can be neglected.

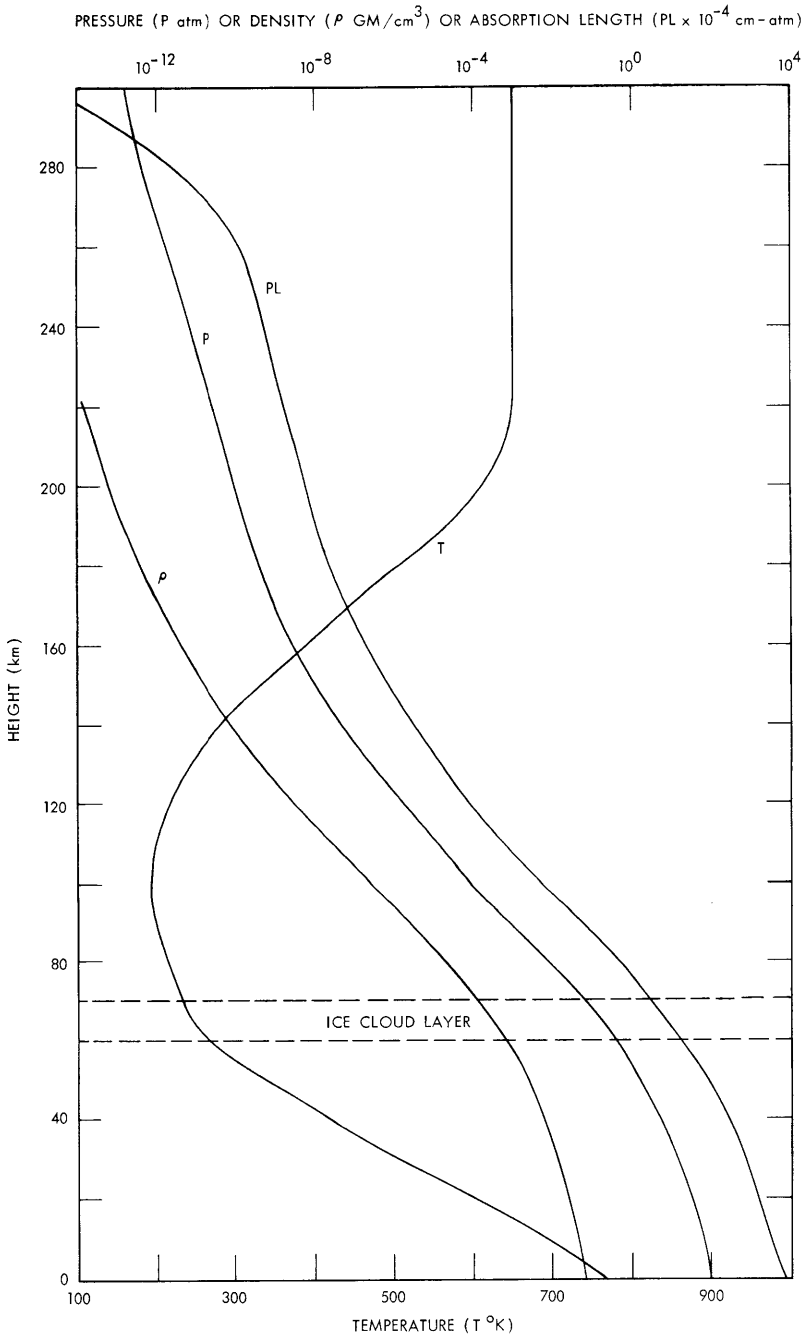

Fig. III-19. Model of the atmosphere of Venus.

The model atmosphere that we adopt is from Marov.[1] Figure III-19 shows profiles for the temperature, T, the pressure, P, and the absorption path, PL, the pressure integrated along the vertical path from 300 km to any height below. The accepted concentration of CO_2 is approximately 95%. As a first approximation, we assume 100% concentration of CO_2 and obtain the density profile shown in Fig. III-19. Integrating this amount gives 6×10^8 cm-atm CO_2 on Venus.

This vast amount of absorbent, compared with 250 cm-atm on Earth, means that Venus is almost opaque in the infrared vibration-rotation bands of CO_2. Instead of using absorption bands to sense the atmosphere of Venus, we may consider the infrared continuum between two bands, or the microwave region. Even then, we find that there is still considerable absorption because of dipole moment induced by high pressure. The lack of a theory for predicting pressure-induced absorption is compensated by laboratory measurements.

2. Infrared Spectrum

Empirical constants have recently been determined for absorption coefficients of CO_2 under high pressure. The opacity τ can be found from

$$\tau = (a_{int} + a_{ind} P)PL, \qquad (1)$$

where P is the gas pressure, and L is the path length. The absorption coefficient a can be intrinsic (int) or pressure-induced (ind). The frequency-dependent values of a are available at fairly high resolution in the intervals 5.5-9.1 μ (Burch and Gryvnak[2]), and 6.4-21 μ (Gal'tsev and Odishariya[3]). In the region 6.4-9.1 μ, agreement is satisfactory between the two sources. For this overlapping region we adopted data from Burch et al.[2] Absorption by isotopic CO_2, which we included in our study, was considered by them[2] but not by Gal'tsev and Odishariya.[3] The "local absorption" at 5.6-6.6 μ was not accounted for by Burch and Gryvnak. We have not included this and, if the effect is real, we may have underestimated the absorption coefficient.

All laboratory data correspond to ~300°K. No quantitative information about the temperature dependence is given. Accordingly, we did not make temperature corrections when we calculated the radiative transfer, and this overestimates the absorption coefficient.

Our laboratory data cover the entire infrared region of interest. CO_2 exhibits few spectral characteristics beyond 21 μ, where the strong rotation band of water is located. Beyond the lower wave number end, absorption is complete owing to the 4.3 and 2.7 μ bands of CO_2. Also important in this range are scattering and radiometer sensitivity.

Within the range 5.5-21 μ, we can determine which frequencies can penetrate the

atmosphere of Venus. From Fig. III-19, the absorption length at the 50-km level is PL = 8×10^5 cm-atm, while the Curtis-Godson[4] scaled pressure is half the actual pressure, or P = 0.7 atm. Equation 1 then selects the frequencies whose α is small enough. For unit opacity τ, only the ranges 5.4-6.7 μ and 8.4-8.9 μ meet this requirement. Frequencies outside these ranges cannot penetrate below the 50-km level even in the absence of cloud cover.

Water vapor does not interfere with the CO_2 continuum around 8.5 μ. In fact, this is the most transparent region for H_2O between the strong ν_2 band at 6.3 μ and the rotation band around 50 μ. The absorption coefficient around 8.5 μ, estimated to be $P^2 f_{H_2O}^2 \times 10^{-9}$ cm^{-1} from the data given elsewhere[5,6] is 10^{-6} lower than for CO_2 if $f_{H_2O} = 0.5\%$. Here f denotes mixing ratio. The CO_2 continuum around 6 μ coincides, however, with the strong 6.3 μ band of H_2O. The absorption of H_2O broadened by CO_2 requires further investigation.

3. Microwave Spectrum

The induced absorption in the microwave region is caused by far wings of lines at much higher frequencies. The absorption coefficient for CO_2 given by Ho et al.[7] is used in this study. The corresponding coefficient given for H_2O is inaccurate at pressures less than a few atm because the resonance at 22.235 GHz must be included, as was done by Barrett and Chung.[8] At high pressure and 300°K temperature the expression[8] for nonresonant absorption by H_2O agrees reasonably with that of Ho et al. We used the entire expression from Barrett et al. It is worth noting that the former coefficient varies as $T^{-3.1}$, the latter as T^{-5}. We therefore allow more absorption at all pressures and temperatures than was predicted by Ho et al.

It is uncertain how much water there is in the atmosphere of Venus. Marov[1] estimates f_{H_2O} to be around 0.5% at the bottom of the cloud. A constant mixing ratio of 0.5% throughout the whole atmosphere amounts to ~245 gm/cm^2, 3/4 of which is contributed by the lowest 21 km. Even for this content the nonresonant absorption coefficient of H_2O alone is approximately half that of CO_2. The omission of H_2O, as by Slade and Shapiro[9] greatly underestimates the total absorption coefficient.

4. Radiative Transfer and Weighting Functions

To calculate radiative transfer in the infrared, we model the cloud by a thin layer at height h above the surface of Venus and characterize it by an effective absorptivity A. The radiance observed at the height H > h is then

$$I = (1-A)\left[B_0 e^{-\tau_0} + \int_0^h B_z e^{-\tau_z} \frac{d\tau_z}{dz} dz\right] + AB_h e^{-\tau_h} + \int_h^H B_z e^{-\tau_z} \frac{d\tau_z}{dz} dz. \qquad (2)$$

Here B_z is the black-body function corresponding to the temperature at height z. The opacity from z to H, τ_z, is calculated by using Eq. 1 and the Curtis-Godson approximation.[4] I, B, and τ are all frequency-dependent. The radiance I is insensitive to cloud parameters at opaque frequencies. At more transparent frequencies, I is more sensitive to a change in A than in h.

On inspecting the two integrals in Eq. 2, we define the weighting function in the presence of cloud as

$$(1-A)\, e^{-\tau_z} \frac{d\tau_z}{dz} \text{ km}^{-1}, \qquad z < h$$

$$e^{-\tau_z} \frac{d\tau_z}{dz} \text{ km}^{-1}, \qquad z > h. \tag{3}$$

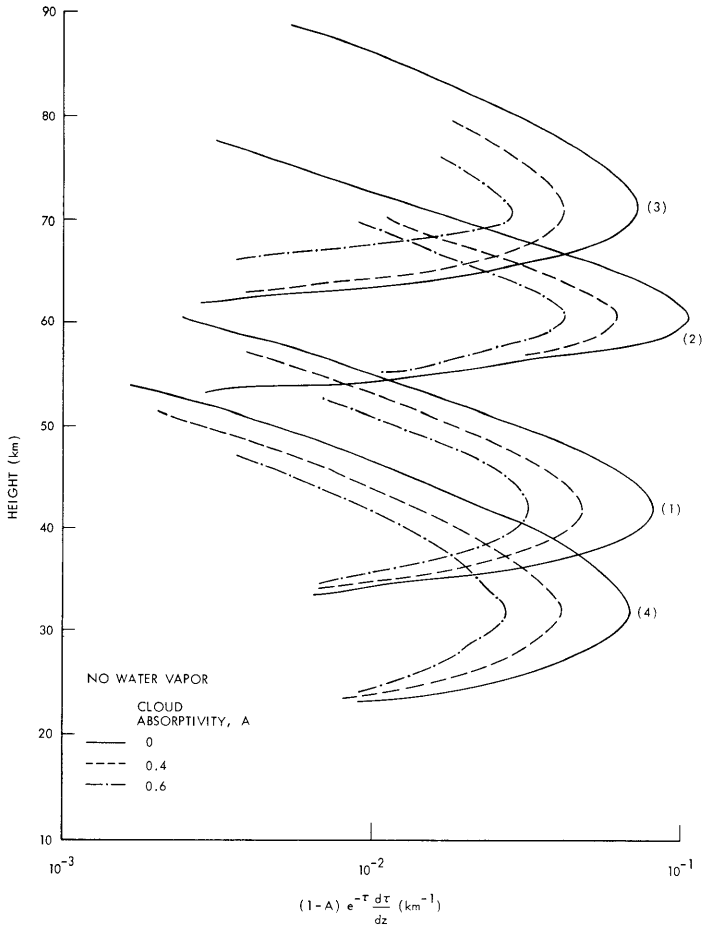

Fig. III-20. Infrared weighting functions at (1) 1140 cm^{-1}, (2) 1300 cm^{-1}, (3) 1380 cm^{-1}, and (4) 1790 cm^{-1}.

Weighting functions at some transparent frequencies are shown in Fig. III-20. No water vapor is assumed. Channels 1, 2, and 3 are little affected if water vapor is present. Channel 4, however, which is most transparent for CO_2, lies in the 6.3 μ band of H_2O.

Microwave radiation is relatively unaffected by the ice cloud. The brightness temperature is

$$T_B = [(1-R)T_0+RT_s]\, e^{-\tau_0} + \int_0^H T_z \left[e^{-\tau_z} + R\, e^{-\tau_0-\tau^z} \right] \alpha_z dz, \qquad (4)$$

where α_z is the absorption coefficient at height z, R is the effective surface reflectivity, $T_s = 3°K$, and τ^z is the opacity from height 0 to z. ($\tau^H = \tau_0$.)

To test our assumption about the water vapor, we investigated its resonance line around 22.235 GHz. Near this frequency $e^{-\tau_0} \cong 0$, and R does not appear as a parameter. The computed brightness temperature is shown in Fig. III-21, which also shows experimental values of Staelin and Barrett[10] and Law and Staelin.[11] A constant mixing ratio of 0.5% is assumed throughout the atmosphere. The water-line dip is not confirmed by experiment, which suggests that the mixing ratio at pressures less than 1 atm

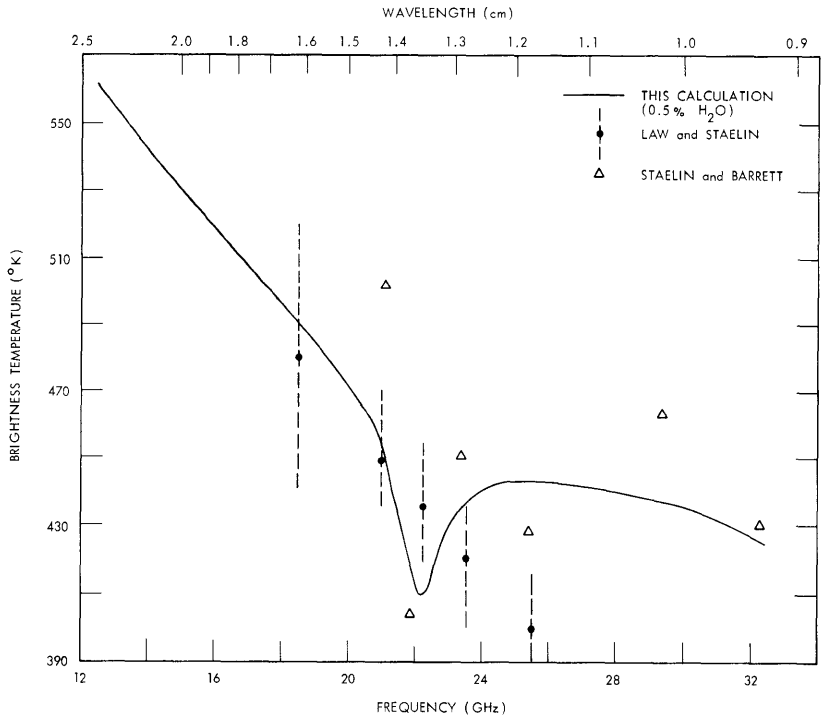

Fig. III-21. Microwave spectrum around 22.235 GHz.

(e.g., above the clouds) is less than 0.5%. Omission of H_2O does not produce the dip, but the corresponding curve (not shown) is generally 70°K higher than the one given here.

Using Eq. 4 with R = 0.151 (Muhleman[12]) and $f_{H_2O} = 0.5\%$, we calculate the brightness temperature for a wider frequency range. The curve is shown in Fig. III-22.

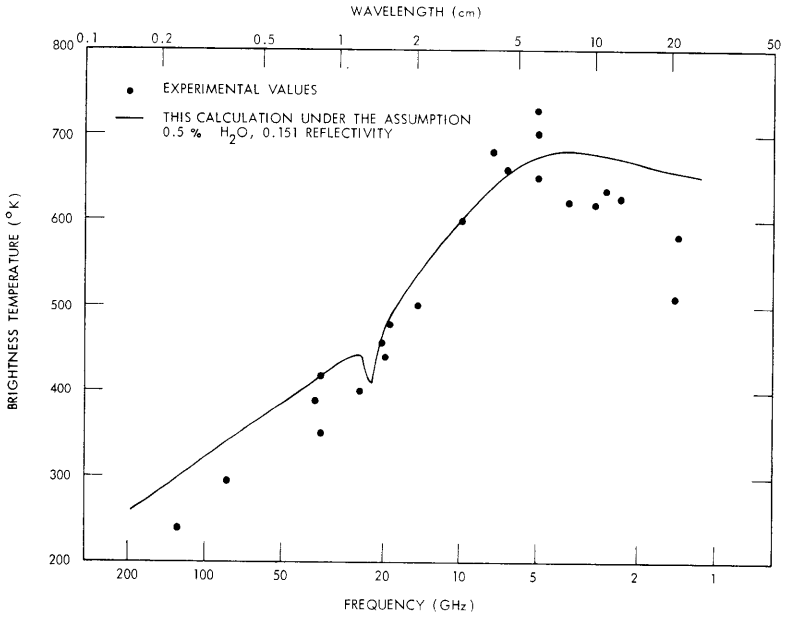

Fig. III-22. Microwave spectrum from 1 GHz to 200 GHz. (Experimental values from Pollack and Morrison.[3]

Pollack and Morrison[13] have collected experimental values from "reliable" sources, and these values with error brackets omitted are reproduced in Fig. III-22 for comparison.

From Eq. 4, we define the weighting function in the microwave region as

$$WF = \left(e^{-\tau_z} + R\, e^{-\tau_0 - \tau^z}\right) a_z \times 10^5 \text{ km}^{-1}, \text{ all } z. \tag{5}$$

Some weighting functions are shown in Fig. III-23. The microwave spectrum is less sensitive than the infrared, as is indicated by its broader spatial extent.

5. Conclusion

A study has been made of radiative transfer on Venus, based on the atmosphere model of Marov.[1] For a nonscattering atmosphere with 100% CO_2, we have reached the following conclusions.

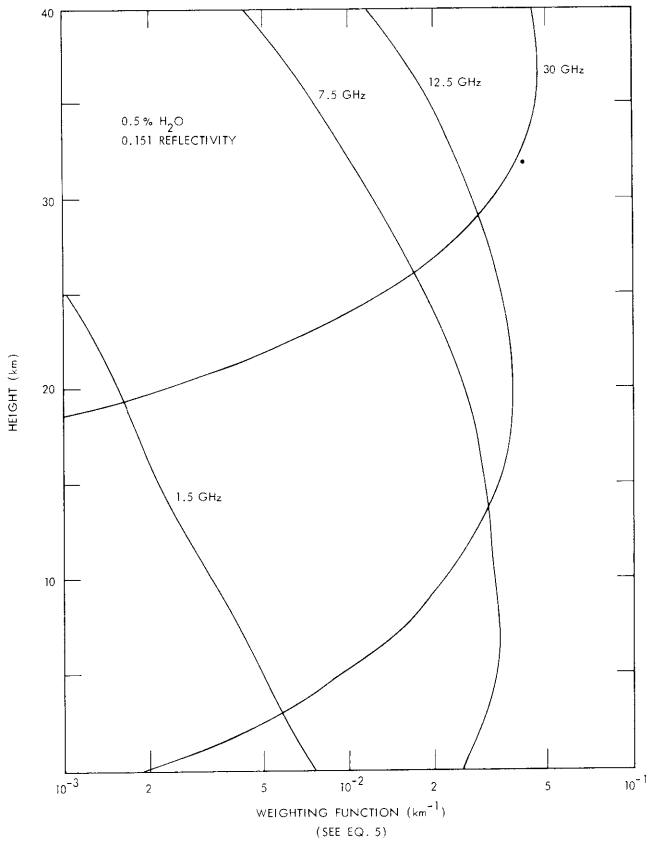

Fig. III-23. Microwave weighting functions.

1. Below 50-km altitude Venus is unobservable beyond 5 μ, except in the CO_2 continua around 5.4-6.7 μ and 8.4-8.9 μ. Pressure-induced absorption limits the penetration of these ranges below the 40-km level.

2. Water vapor is transparent in the 8.4-8.9 μ continuum. The 6.3 μ band of water vapor might interfere with the 5.4-6.7 μ CO_2 continuum.[14]

3. Despite pressure-induced absorption, microwave frequencies are more penetrative than infrared. If 0.5% water vapor is present, its absorption is not negligible compared with 100% CO_2.

4. For the most transparent channels in the infrared, weighting functions are as indicated in Fig. III-20 where no water vapor is assumed and a thin layer of ice cloud is characterized by its height and absorptivity.

5. The assumption of 0.5% water vapor is not inconsistent with microwave observations (Fig. III-21). Weighting functions with this content assumed are shown in Fig. III-23.

R. K. L. Poon, D. H. Staelin

References

1. M. Ya. Marov, "A Model of the Venus Atmosphere," Dokl. Akad. Nauk SSSR 196, 67-70 (1971).

2. D. E. Burch and D. A. Gryvnak, "Absorption by CO_2 between 1100 and 1835 cm^{-1}," J. Opt. Soc. Am. 61, 499-503 (1971).

3. A. P. Gal'tsev and M. A. Odishariya, "The CO_2 Absorption Bands of 7.2, 7.8, 9.4, 10.4, and 15 μ at High Pressures," Izv. Akad. Nauk SSSR, Fizi. Atmos. I Okeana 6, 881-888 (1970).

4. W. L. Godson, "The Computation of Infrared Transmission by Atmospheric Water Vapor," J. Meteorol. 12, 272-283 (1955).

5. K. Bignell, F. Saiedy, and P. A. Sheppard, " On the Atmospheric Infrared Continuum," J. Opt. Soc. Am. 53, 466-479 (1963).

6. J. H. McCoy, D. B. Rensch, and R. K. Long, "Water Vapor Continuum Absorption of CO_2 Laser Radiation near 10 μ," Appl. Opt. 8, 1471-1478 (1969).

7. W. Ho, I. A. Kaufman, and P. Thaddeus, "Laboratory Measurement of Microwave Absorption in Models of the Atmosphere of Venus," J. Geophys. Res. 71, 5091-5108 (1966).

8. A. H. Barrett and V. K. Chung, "A Method for the Determination of High-Altitude Water-Vapor Abundance from Ground-Based Microwave Observations," J. Geophys. Res. 67, 4259-4266 (1962).

9. M. A. Slade and I. I. Shapiro, "Interpretation of Radar and Radio Observations of Venus," J. Geophys. Res. 75, 3301-3317 (1970).

10. D. H. Staelin and A. H. Barrett, "Spectral Observations of Venus near 1-Centimeter Wavelength," Astrophys. J. 144, 352 (1966).

11. S. E. Law and D. H. Staelin, "Measurements of Venus and Jupiter near 1 Cm Wavelength," Astrophys. J. 154, 1077-1086 (1968).

12. D. O. Muhleman, "Microwave Opacity of the Venus Atmosphere," Astron. J. 74, 57-69 (1969).

13. J. B. Pollack and D. Morrison, "Venus: Determination of Atmospheric Parameters from the Microwave Spectrum," Icarus 12, 376-401 (1970).

14. Recent data from D. E. Burch (Philco Technical Report, 1970) indicate that we have far underestimated the absorption of water vapor in the CO_2 continua. Our second conclusion therefore needs revision.